The Astrophysical Journal, 1004:154 (16pp), 2026 June 20 https://doi.org/10.3847/1538-4357/ae5d49
© 2026. The Author(s). Published by the American Astronomical Society.
OPEN ACCESS

Variable X-Ray Sources Associated with Extragalactic Supernova Remnants

Andrea H. Prestwich[1,2,3], Francis Primini[4,7], Roy E. Kilgard[5], Nanda Rea[6], and Michael L. McCollough[4]
[1] Institute for Astrophysics and Computational Sciences, The Catholic University of America, Washington, DC 20064, USA
[2] Astrophysics Science Division, NASA Goddard Space Flight Center, Greenbelt, MD 20771, USA
[3] Center for Research and Exploration in Space Science and Technology, NASA Goddard Space Flight Center, Greenbelt, MD 20771, USA
[4] Center for Astrophysics (CfA), Smithsonian Astrophysical Observatory, B-240, 60 Garden St., Cambridge, MA 02138, USA
[5] Astronomy Department and Van Vleck Observatory, Wesleyan University, Middletown, CT 06459, USA
[6] Institute of Space Sciences (ICE, CSIC), Campus UAB, Carrer de Can Magrans s/n, 08193, Barcelona, Spain
Received 2025 August 21; revised 2026 March 19; accepted 2026 March 26; published 2026 June 11

Abstract

We report a serendipitous and unexpected discovery from a study of long-term X-ray variability in the nearby galaxy M83: a substantial fraction of X-ray sources classified as supernova remnants (SNRs) exhibit significant variability. This behavior is surprising because soft X-ray emission from remnants older than ∼100 yr is generally expected to evolve smoothly, with little variation on decade-long timescales. At least one source in our sample is associated with the historical supernova SN 1957D, for which the X-ray emission and variability are well explained by shock interaction between the expanding ejecta and the surrounding circumstellar medium. For most sources, however, the observed variability is difficult to reconcile with standard models of SNR evolution. Instead, the light curves and spectra are more naturally explained by the presence of an accretion-powered source coincident with the remnant. Plausible explanations include fallback accretion onto the compact object formed in the SN explosion or an X-ray binary physically associated with the remnant. The variable X-ray sources are statistically correlated with high-mass stars, indicating potential donor stars and supporting a high-mass X-ray binary interpretation. Their luminosities and spectral properties are also consistent with emission from cool accretion disks around stellar-mass black holes. Although the current data do not uniquely determine the nature of these systems, the results suggest that accretion-powered sources associated with SNRs may be more common than previously recognized.

Unified Astronomy Thesaurus concepts: High mass x-ray binary stars (733); Massive stars (732); Supernova remnants (1667); Black holes (162); Compact objects (288); Stellar remnants (1627); X-ray astronomy (1810); X-ray binary stars (1811)

Materials only available in the online version of record: figure sets, machine-readable table

1. Introduction

Nearby galaxies contain a multitude of X-ray sources. One of the great legacies of the Chandra X-ray Observatory is that it can resolve discrete sources from diffuse emission in nearby galaxies, allowing X-ray sources to be classified and associated with known objects at other wavelengths (e.g., R. E. Kilgard et al. 2001; M. Lazzarini et al. 2023). This has led to advances in understanding how X-ray populations are related to fundamental galaxy parameters such as mass and star formation (V. Antoniou et al. 2009; B. D. Lehmer et al. 2013, 2024) and how such populations evolve over time (T. Fragos et al. 2013, 2023; D. Misra et al. 2023). In star-forming and starburst galaxies, the dominant compact X-ray sources are high-mass X-ray binaries (HMXBs) and core-collapse supernova remnants (SNRs; K. S. Long et al. 2010; R. Chandar et al. 2020; Q. Hunt et al. 2021).

High-mass X-ray binaries consist of a neutron star or black hole accreting material from a massive stellar companion, and are among the most variable X-ray sources known. Their X-ray emission exhibits variability over a wide range of timescales (R. Kyer et al. 2024). Observations of individual systems show that black hole X-ray binaries undergo outbursts lasting from ∼20 days to several months (R. A. Remillard & J. E. McClintock 2006). Additional variability is observed on orbital timescales (hours to days) and on superorbital timescales (tens to hundreds of days; F. Fürst et al. 2019). Moreover, HMXBs commonly display aperiodic variability spanning seconds to days, which is generally attributed to fluctuations in the accretion rate and/or changes in the line-of-sight absorbing column (F. Fürst et al. 2019).

Soft X-ray emission from black hole binaries typically arises from the outer regions of the accretion disk, where the gas is heated to temperatures of around 10^5–10^7 K (M. Gierliński & C. Done 2003, 2004; J. E. McClintock & R. A. Remillard 2006). The spectrum of soft X-rays often follows a characteristic power-law or multicolor disk emission model, which is thought to be a combination of thermal emission from the accretion disk and Comptonized radiation from the inner regions (C. Done & A. Kubota 2006). In particular, the soft X-ray flux is observed to vary with the state of the binary system, with brighter soft X-rays being linked to the disk-dominated "high" state, where the disk extends closer to the black hole (J. E. McClintock & R. A. Remillard 2006).

Core-collapse supernovae mark the terminal explosion of massive stars. The stellar core collapses to form either a neutron star or a black hole (H.-T. Janka 2012), with the outcome determined by a combination of factors including the

[7] Retired.

Original content from this work may be used under the terms of the Creative Commons Attribution 4.0 licence. Any further distribution of this work must maintain attribution to the author(s) and the title of the work, journal citation and DOI.

progenitor mass, rotation, and magnetic fields. The subsequent evolution of the remnant can also be strongly influenced by fallback accretion in the immediate aftermath of the explosion (e.g., F. C. Michel 1988; R. A. Chevalier 1989; A. D. Khokhriakova & S. B. Popov 2022). In this process, a fraction of the ejected material fails to escape the gravitational potential of the newly formed compact object and instead falls back, accreting onto the remnant. Such fallback is expected when the explosion energy is insufficient to unbind the entire stellar envelope. Fallback accretion can substantially modify supernova (SN) light curves on short timescales of days (J. Dexter & D. Kasen 2013), and on longer timescales the infalling material is expected to circularize and form an accretion disk (e.g., M. Ronchi et al. 2022). Fallback accretion has been widely invoked to explain the early-time evolution of SNe (L. J. Wang et al. 2018) and gamma-ray bursts (S. L. Gibson et al. 2018), typically on timescales of up to $\sim$1 yr.

Supernova remnants in nearby galaxies are usually identified as optical emission-line regions (K. S. Long 2017). Because SNe ejecta are shock-heated to $\sim 10^6$ K many remnants are soft thermal X-ray sources (M. Sasaki et al. 2012). The X-ray evolution of a SN, from the time of the explosion to a hot gaseous remnant, has been extensively studied in recent years. In the years to decades after the explosion, the SNe is often detected as a bright, soft X-ray source (S. Immler et al. 2005; S. Chakraborti et al. 2016). At this stage, the X-ray emission is thought to arise from shocks in the circumstellar material ejected by the progenitor star before it exploded (e.g., S. Chakraborti et al. 2016). V. Ramakrishnan & V. V. Dwarkadas (2020) explored the X-ray light curves of several historical SNe to understand the transition from SNe (expanding into the circumstellar material) to SNRs (expanding into the interstellar medium (ISM)). They found that the X-ray light curves gently decline over the first 50 yr and then increase during the free-expansion phase as the volume of swept-up interstellar material increases (see their Figure 16).

M83 (the Southern Pinwheel) is a nearby (4.66 Mpc; A. Saha et al. 2006), nearly face-on ($i = 24°$; R. J. Talbot et al. 1979) spiral galaxy characterized by active star formation along its spiral arms and a central nuclear starburst (e.g., A. Wofford et al. 2011; A. Adamo et al. 2015). The global star formation rate is 3–4$\dot{M}$ per year (S. Boissier et al. 2005). The high star formation rate has resulted in a large and well-studied population of SNRs (e.g., K. S. Long et al. 2010, 2014; P. F. Winkler et al. 2017). In a recent study, Q. Hunt et al. (2021) classified compact X-ray sources detected with Chandra in M83 as low-, intermediate-, or high-mass X-ray binaries, based on the locations of candidate optical counterparts in color–magnitude diagrams and the estimated ages of associated star clusters. The primary goal of that work was to calibrate the X-ray luminosity function of the X-ray binary population. To construct a clean sample, sources identified as SNRs in the catalog of K. S. Long et al. (2014) were explicitly excluded.

In the present work, we report a serendipitous result that emerged from an investigation of the long-term variability of the Q. Hunt et al. (2021) source sample: We find that a substantial fraction of the X-ray sources classified as SNRs by K. S. Long et al. (2014) exhibit significant variability. The remnants considered here are predominantly older objects, likely in the free-expansion phase, for which X-ray variability on timescales of $\sim$10 yr is not generally expected. The two most plausible explanations for X-ray variability associated with SNRs are that the remnants are extremely young or that the variability arises from an accreting source coincident with the nebula. This paper presents evidence for X-ray variability in SNRs in M83 and considers plausible origins for this variability, including young, rapidly evolving SNRs, fallback accretion onto a compact object, and emission from a HMXB.

The outline of the paper is as follows. In Section 2, we describe the SNR sample and data from the Chandra Source Catalog (CSC). In Section 3, we present evidence that the sample sources are variable. In Section 4, we demonstrate that the X-ray sources in our sample are genuinely associated with SNRs and not the result of chance coincidence. In Section 5, we model the X-ray spectra, and in Section 6, we identify the spectral components that drive the observed variability. In Section 7, we discuss possible origins of the variability, including variability from young SNe, X-ray emission from HMXBs, and possible fallback accretion. Finally, we summarize our conclusions in Section 8.

2. Data and Sample Selection

Our primary source for variability data—including X-ray photometry, spectral measurements, variability properties, and associated data products, is the CSC (I. N. Evans et al. 2024). As discussed in Section 1, the primary goal of Q. Hunt et al. (2021) was to calibrate the X-ray luminosity function of the X-ray binary population. To accomplish this, they excluded sources identified as SNRs using the catalog of K. S. Long et al. (2014). These excluded sources constitute the main sample analyzed in the present work. Optical counterparts were identified by Q. Hunt et al. (2021) using Hubble Space Telescope (HST) Wide Field Camera 3 UVIS imaging, which covers a mosaic of $\sim$43 arcmin^2. Figure 1 of Q. Hunt et al. (2021) shows the optical field with detected X-ray sources overlaid.

Chandra obtained 13 ACIS observations of M83 between 2000 and 2014, as summarized in Table 1. To investigate the variability of sources analyzed by Q. Hunt et al. (2021), we cross-matched their catalog against the CSC. To ensure full coverage of the optical footprint, we selected CSC sources within 7′ of the center of M83 that satisfy the following criteria:

1. *Master source significance >3.* Within the CSC, each distinct X-ray source is represented by a unique *master source*. The reported source properties (e.g., position, flux, and detection significance) are derived from an observation stack in which observations obtained with the same instrument are coadded prior to source detection (I. N. Evans et al. 2024). This stacking procedure increases the signal-to-noise ratio relative to individual observations and enables the detection of fainter sources. To minimize contamination by spurious detections due to background fluctuations, we restrict our sample to master sources with a source significance greater than 3.
2. *Dither, pileup, and streak flags set to* `FALSE`. Sources were excluded if the ACIS pileup fraction exceeded $\sim$10% in all observations, as pileup can significantly distort the measured X-ray spectrum. We also rejected

Table 1
Chandra ACIS Observations Included in This Study

Obs ID	Instrument	Exposure (ks)	Observation Date (yyyy-mm-dd)
793	ACIS-S	50.98	2000-04-29
2064	ACIS-S	9.84	2001-09-04
12995	ACIS-S	59.29	2010-12-23
13202	ACIS-S	98.78	2010-12-25
12993	ACIS-S	49.4	2011-03-15
13241	ACIS-S	78.96	2011-03-18
12994	ACIS-S	150.06	2011-03-23
12996	ACIS-S	53.04	2011-03-29
13248	ACIS-S	54.33	2011-04-03
14332	ACIS-S	52.38	2011-08-29
12992	ACIS-S	66.29	2011-09-04
14342	ACIS-S	67.1	2011-12-28
16024	ACIS-I	29.59	2014-06-07

sources that fall on an ACIS readout streak in all observations, since this can compromise the derived source properties. We also excluded sources flagged for dither-related variability. This warning is triggered when the strongest peak in the source-region power spectrum coincides with the spacecraft dither frequency, or a related beat frequency, in one or more observations, potentially producing spurious variability.

3. *Confusion flag set to* `FALSE`. Sources with the confusion flag set were excluded. This flag indicates that source extraction regions overlap in one or more contributing stacked observations. Overlapping regions can lead to unreliable photometry and spurious variability detections.

This selection yielded 133 sources, 43 of which are classified as SNRs in Q. Hunt et al. (2021). These sources are listed in the Appendix (Table 7). All catalog cross-matching and data manipulation were performed with `TOPCAT` v4.9–4.9 (M. B. Taylor 2020).

3. Evidence for Variability

The CSC provides several diagnostics for X-ray variability, including tests sensitive to both intra-observation and inter-observation flux changes. Variability between observations is quantified by the parameter `var_inter_prob`, which gives the probability that a source varies across epochs. Throughout this paper, we denote `var_inter_prob` by $P_{\rm var}$, and report values separately for each of the standard CSC energy bands (e.g., $P_{\rm var}(b)$ for the broad band and $P_{\rm var}(s)$ for the soft band). The inter-observation variability probability is derived from a χ^2 test that assesses whether the photon fluxes measured in individual observations are consistent with a constant source flux (I. N. Evans et al. 2024). A high value of $P_{\rm var}$ implies that the null hypothesis of constant intrinsic flux is unlikely. However, $P_{\rm var}$ is not simply related to the fractional amplitude of variability: Small fractional changes can yield high $P_{\rm var}$ values when flux uncertainties are small, whereas large fractional changes may produce low $P_{\rm var}$ values if the uncertainties are substantial.

The dataset spans approximately 14 yr but is characterized by highly uneven temporal sampling. Two early observations, separated by roughly 16 months, are followed by a nearly decade-long gap. The cadence then increases dramatically in 2010–2011, when multiple observations were obtained on timescales of days to months, before another multiyear gap leading to the final epoch in 2014. As a result, the data probe variability on several distinct timescales: long-term evolution over a decade, intermediate changes over months, and short-term variations over a few days during the intensive 2011 campaign. However, the extended gaps between observing periods limit our ability to track continuous behavior or constrain variability on intermediate timescales that are not directly sampled.

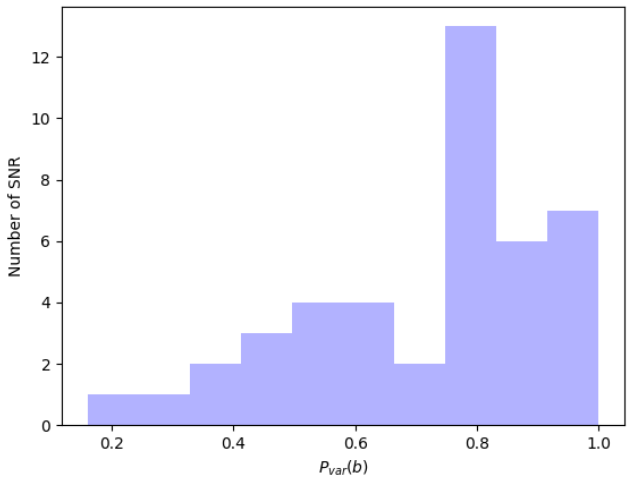

Figure 1. Distribution of $P_{\rm var}(b)$ for the SNR sample.

Figure 1 shows the distribution of $P_{\rm var}(b)$ for the 43 soft X-ray sources coincident with SNRs and lying within the HST footprint. Corresponding $P_{\rm var}(b)$ and $P_{\rm var}(s)$ values are listed in Table 7 in the Appendix. The distribution is not consistent with a population of constant-flux sources, as would be expected if the emission arises from thermal plasma in evolved remnants. Light curves for these 43 sources are shown in Figure 2.

We define sources with the strongest statistical evidence for variability ($P_{\rm var}(b)$ or $P_{\rm var}(s) \geqslant 0.8$) as high-probability variables (Table 2). This threshold was adopted to select sources that are likely to be genuinely variable while limiting contamination from statistical fluctuations. With this criterion, 22 sources—approximately half the sample—are classified as high-probability variables, with ∼2 sources expected to be nonvariable based on the adopted probability threshold. Within this subset, two distinct patterns emerge. The first group displays comparatively high fluxes in 2000 followed by a gradual decline over the subsequent ∼13 yr (slow decline, SD), a behavior characteristic of young SNe (Section 1). The second group undergoes substantial flux changes at one or more epochs but shows no coherent long-term trend (flare sources).

3.1. Comparison with Previous Work

In this section, we compare the variability measures provided by the CSC with previous assessments in the literature. Because significant variability in M83 SNRs is not generally anticipated, it is important to demonstrate consistency between the CSC variability statistics and earlier analyses.

K. S. Long et al. (2014) examined variability for all X-ray sources in M83—without restricting the sample to SNRs—by comparing the time-averaged flux of each source with its flux

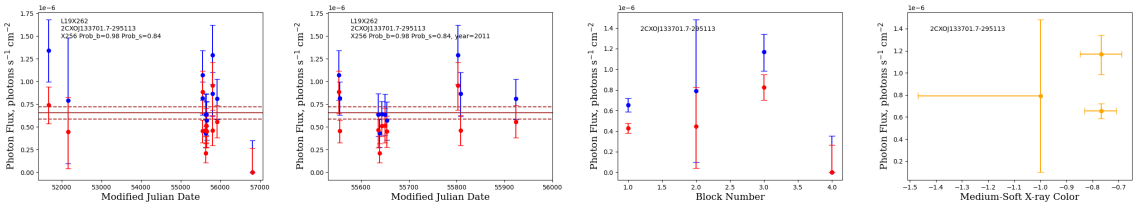

Figure 2. Example light curve for 2CXOJ133701.7−295113. From left to right: (1) Photon flux as a function of time for the entire period 2000–2014. The blue indicates the broadband flux, and the red indicates the soft flux. (2) Light curve as described for (1), but restricted to 2011, when a number of observations were obtained. (3) Broadband (blue) and soft (red) flux blocks. (4) Medium–soft X-ray color vs. photon flux for flux blocks with sufficient counts to measure a color. The complete figure set (43 images) is available in the online journal.

(The complete figure set (43 images) is available in the online article.)

Table 2
Sources with the Highest Likelihood of X-Ray Variability ($P_{\rm var}(b)$ or $P_{\rm var}(s) \geqslant 0.8$)

CSCID	$P_{\rm var}(b)$	$P_{\rm var}(s)$	Light-curve Type
2CXOJ133648.3−295244	0.75	0.81	Flare
2CXOJ133652.8−295110	0.94	0.6	Flare
2CXOJ133653.2−295133	1.0	1.0	Flare
2CXOJ133653.8−294848	0.88	0.49	SD
2CXOJ133655.0−295239	0.87	0.41	SD
2CXOJ133655.1−295040	0.8	0.8	Flare
2CXOJ133655.5−295303	1.0	0.87	Flare
2CXOJ133657.8−295303	0.81	0.13	SD
2CXOJ133658.7−295100	0.84	0.42	Flare
2CXOJ133659.8−295526	0.82	0.58	Flare
2CXOJ133700.4−295323	0.83	0.90	Flare
2CXOJ133701.7−295113	0.98	0.84	Flare
2CXOJ133702.4−295126	0.88	0.25	SD
2CXOJ133703.4−295401	0.85	0.87	Flare
2CXOJ133706.1−295444	1.0	0.95	SD
2CXOJ133706.4−295025	0.83	0.81	Flare
2CXOJ133706.6−295332	0.94	0.84	Flare
2CXOJ133707.0−295321	0.76	0.83	Flare
2CXOJ133708.3−295056	0.59	0.82	Flare
2CXOJ133708.5−295135	0.84	0.74	Flare
2CXOJ133708.7−295137	0.93	0.94	Flare
2CXOJ133710.9−295046	0.8	0.64	Flare

Note. The "Light-curve Type" column denotes the inferred variability behavior, classified as either flare-type (Flare) or slow decline (SD).

in individual observations. Sources whose fluxes were inconsistent with a constant value at the 3σ (99.7%) level were classified as variable. Figure 3 shows the distribution of $P_{\rm var}(b)$ for the full Q. Hunt et al. (2021) sample, with the sources identified as variable by K. S. Long et al. (2014) highlighted. As in K. S. Long et al. (2014), this figure includes all detected X-ray sources and is not limited to SNR candidates.

The sources classified as variable by K. S. Long et al. (2014) have an average $P_{\rm var}(b)$ of 0.99, spanning 0.95–1.0. Thus, the objects identified as variable at the 3σ level by K. S. Long et al. (2014) correspond closely to those flagged at $\gtrsim$99% probability in the CSC, demonstrating strong agreement between the independent approaches.

By contrast, most SNRs in our sample were not classified as "variable" by K. S. Long et al. (2014). This primarily reflects the more stringent 3σ (99.7%) criterion adopted in that study, which selects only the most strongly variable sources. Four SNRs have $P_{\rm var}$ values in the highest bin of Figure 3 (0.95–1.0): 2CXOJ133653.2−295133, 2CXOJ133655.5−295303, 2CXOJ133701.7−295113, and 2CXOJ133706.1−295444. Of these, 2CXOJ133655.5−295303 was identified as variable by K. S. Long et al. (2014). The remaining differences likely reflect the inclusion of the 2014 observation in the CSC, which was not available at the time of the earlier analysis.

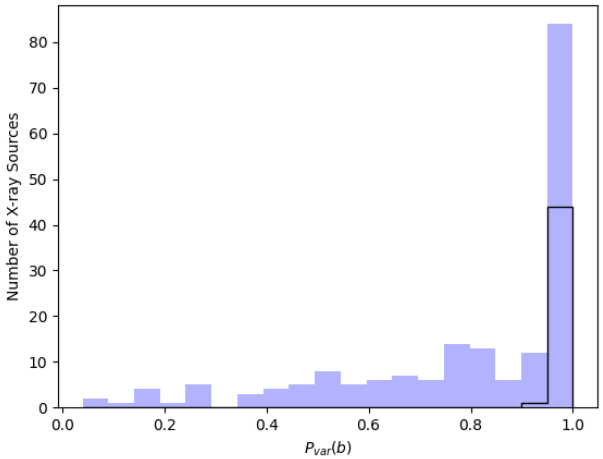

Figure 3. Histogram showing the distribution of $P_{\rm var}(b)$ for the full Q. Hunt et al. (2021) sample (not just SNRs) compared to $P_{\rm var}(b)$ for sources identified as variable by K. S. Long et al. (2014, black line).

4. Association of Soft X-Ray Sources with SNRs

Soft X-ray sources are ubiquitous in star-forming galaxies (R. Di Stefano et al. 2004; A. H. Prestwich et al. 2009; I. Galiullin & M. Gilfanov 2021), as are SNRs; however, the two populations do not always overlap. Many soft sources lack SNR counterparts, and many SNRs are undetected in X-rays (e.g., L. A. Maddox et al. 2006; C. J. Stockdale et al. 2006). Several authors have argued that soft and quasi-soft X-ray sources may correspond to SNRs even in the absence of the traditional optical or radio shock diagnostics (I. Galiullin & M. Gilfanov 2021). It is therefore essential to establish whether the soft sources in our sample are physically associated with known SNRs rather than spatial coincidences.

In this section, we (1) identify a comparison sample of soft X-ray sources with properties similar to our SNR candidates, (2) test whether these soft sources are statistically associated with known SNRs, and (3) confirm that the optical and radio emission used to classify these objects is consistent with shock

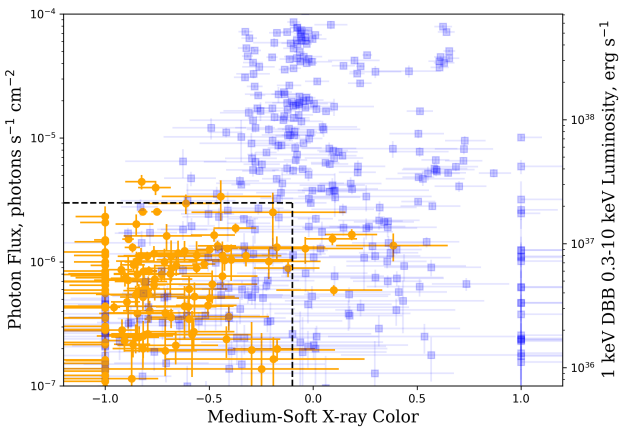

Figure 4. Medium–soft color (HR_{MS}) vs. photon flux for X-ray sources in M83 from Q. Hunt et al. (2021). Sources classified as SNR are shown as orange circles, while all other source types are shown as blue squares. For reference, the right-hand axis indicates the corresponding 0.3–10 keV luminosity for a disk blackbody with $T_{in} = 1$ keV. The black dashed lines outline the region of the flux–color plane used to define the "soft" comparison sample.

excitation rather than photoionization, ruling out misclassification of bright H II regions as SNRs.

4.1. Selecting Soft Sources: Flux-block Diagrams

Within the CSC, a *flux block* is constructed by grouping together observations whose measured fluxes are statistically consistent, such that a single block may comprise multiple observations. This approach allows data obtained while a source is in a common flux state to be combined, thereby improving the signal-to-noise ratio. The flux-block framework was developed to support analyses of sources with flux-dependent spectral behavior (e.g., X-ray binaries) and uses a Bayesian algorithm to identify statistically significant changes in flux (I. N. Evans et al. 2024).

For each source, we construct a *flux-block diagram* plotting photon flux against medium–soft color for the individual flux blocks. The medium–soft color is defined as $HR_{MS} = \frac{M-S}{M+S}$, where "M" and "S" are the photon fluxes in the medium (1.2–2 keV) and soft (0.5–1.2 keV) bands, respectively. All X-ray hardness ratios and their upper and lower bounds are taken from the CSC. The flux-block diagram for all sources in the Q. Hunt et al. (2021) sample is shown in Figure 4.

We define a comparison sample of 103 soft X-ray sources with properties similar to those of our primary sample. The sample is selected by requiring $HR_{MS} < -0.1$ and photon flux $<3 \times 10^{-6}$ photons cm^{-2} s^{-1}, thresholds that encompass the region occupied by the SNR candidates (black dashed lines in Figure 4). Sources were drawn from the CSC v2.1 catalog within 7′ of the M83 nucleus using the same quality criteria described in Section 2. Cross-matching this set with the K. S. Long et al. (2014) SNR catalog yields 72 associations. Because the 7′ search radius extends beyond the HST footprint, the comparison sample includes the primary sample but is larger than the subset restricted to the optical mosaic.

To assess the probability of chance alignment, we repeated the cross-match after shifting each X-ray position by 10″ in a random direction. No matches were recovered in any realization, indicating that the soft sources are not spatially coincident with SNRs by chance.

Finally, we verify that the optical/radio emission used to identify these SNRs originates in shock-heated gas. K. S. Long et al. (2022) used MUSE/Very Large Telescope spectroscopy to confirm the diagnostic power of the Si[II]:Hα ratio: values >0.4 indicate shocked gas, while lower ratios are consistent with photoionized H II regions (see also P. F. Winkler et al. 2017). Of our 43 SNR candidates, 39 have MUSE coverage. Only three have Si[II]:H$\alpha < 0.4$ (2CXOJ133700.1−294810, 2CXOJ133703.5−294940, and 2CXOJ133710.9−295046). We therefore suggest that the optical nebulosity associated with the variable X-ray sources arises from shocked gas in SNRs, and that misidentified H II regions are unlikely to contaminate our sample.

5. X-Ray Spectroscopy: Evidence for an Accretion Disk

As noted in Section 1, the two most plausible explanations for X-ray variability associated with SNRs are that the remnants are extremely young or that the variability originates from an accreting source coincident with the nebula. If an accreting compact object is present, its X-ray spectrum should show signatures consistent with emission from an accretion disk. To test this possibility, we fit the spectra of individual sources with simple phenomenological models representative of (1) an accretion disk, (2) shock-heated gas, and (3) a combination of the two.

1. All sources were fit with a disk blackbody (DBB) model, which is commonly used to describe emission from a cool, optically thick accretion disk and is often associated with black hole binaries. The DBB model represents the spectrum as a superposition of multicolor blackbody components and is characterized by two parameters: r_{in}, the innermost disk radius, and T_{in}, the effective temperature at r_{in} (K. Mitsuda et al. 1984). This model is not generally applicable to accretion onto a neutron star, where additional emission from the stellar surface or boundary layer is expected (see T. J. Maccarone et al. 2016 and references therein).
2. All sources were also fit with a nonequilibrium ionization (NEI) model, which is characteristic of shock-heated plasma (see K. J. Borkowski et al. 2001 and references therein). The NEI models developed by K. J. Borkowski et al. (2001) are designed to describe the spatially integrated X-ray emission from SNRs and are based on Sedov–Taylor dynamics. The resulting spectra depend on the elemental abundances and on three key physical parameters: the postshock electron temperature, the postshock density, and the ionization timescale.
3. Sources with >150 total counts were additionally fit with a combined DBB+NEI model, allowing for both disk emission and thermal emission from hot gas in the remnant. This model is not applied to lower-count sources because the number of free parameters would approach or exceed the number of degrees of freedom (dof).

All spectral fits were performed using data products from the CSC, including source and background pulse-height amplitude files and the associated response files: the auxiliary response file (or ARF) and the redistribution matrix file (or RMF). Because the number of counts in any single observation is low, spectra were constructed by combining all available observations for each source. As a result, the fitted spectra

Table 3
Representative Spectral Fit Parameters for All Sources

Source	Counts	DBB			NEI			NEI+DBB		
		T_{in}	χ^2/dof	kT	τ	χ^2/dof	T_{in}	kT	τ	χ^2/dof
2CXOJ133650.8–295240	252.63	0.146	14.99/26	1.14	0.075	11.42/25	0.949	0.712	0.115	11.48/23
2CXOJ133652.8–295231	304.78	0.252	32.27/26	4.262	0.263	17.94/25	0.660	0.827	0.901	15.71/23
2CXOJ133653.8–294848	277.64	0.138	29.02/20	1.03	0.058	14.73/19	0.0	1.03	0.058	14.73/17
⋮	⋮	⋮	⋮	⋮	⋮	⋮	⋮	⋮	⋮	⋮

Note. Temperatures are in keV and τ is in units of 10^{11} s^{-1} cm^{-3}. Confidence bounds and fit probabilities are omitted here for readability and are included in the machine-readable table.

(This table is available in its entirety in machine-readable form in the online article.)

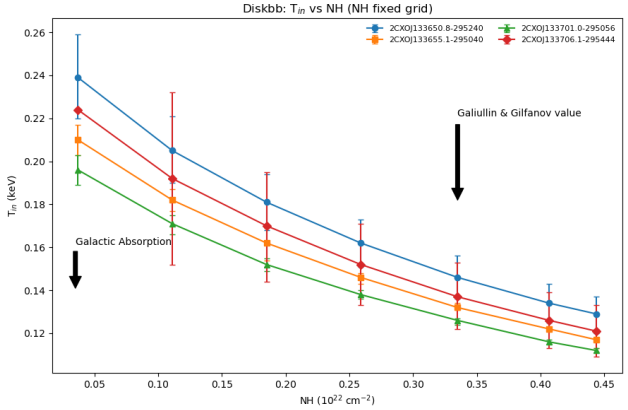

Figure 5. Fitted inner disk temperature (T_{in}) as a function of assumed absorption column density for four representative X-ray sources in our sample. The Galactic line-of-sight absorption toward M83 and the value adopted by I. Galiullin & M. Gilfanov (2021) are indicated for reference. The derived T_{in} values show a clear dependence on the assumed absorption.

represent an average over all flux states in the flux-block color diagram.

Spectral modeling was carried out with `sherpa` version 4.17 (A. Siemiginowska et al. 2024), using the `chi2gehrels` statistic. Background spectra were subtracted, and the data were grouped to a minimum of 15 counts per spectral bin. Parameter uncertainties correspond to 1σ (68.27%) confidence intervals and were estimated using the covariance method implemented in `sherpa`.

Preliminary fits allowing the line-of-sight absorption column density (N_H) to vary revealed strong degeneracies between N_H and the DBB inner disk temperature (T_{in}). To quantify this effect, we refit four representative sources using a range of fixed N_H values. The lowest value corresponds to the Galactic line-of-sight absorption toward M83, while the highest is 12 times this Galactic value. As shown in Figure 5, the fitted T_{in} depends strongly on the assumed N_H, with T_{in} decreasing systematically as N_H increases. A similar dependence was reported by I. Galiullin & M. Gilfanov (2021), who adopted a fixed value of $N_H = 3.35 \times 10^{21}$ cm^{-2} to account for both atomic and molecular gas along the line of sight in M83. We therefore fix N_H to this value in our spectral fits.

With N_H held fixed, the remaining free parameters were as follows. For the DBB model, the inner disk temperature (T_{in}) and normalization were allowed to vary. For the NEI model, the plasma temperature, ionization timescale, and normalization were free parameters, while the elemental abundances were fixed at solar and the redshift was set to zero. This choice of N_H places the fitted T_{in} values toward the lower end of the range spanned by plausible absorption values.

Detailed fitted parameters are given in Table 3, and plots showing the fitted spectra and residuals for all models are shown in Figure 6. The results are summarized in Table 4. The parameter Q_{val} gives the probability of obtaining the reduced χ^2 value, or a larger one, assuming the model is correct and the fitted parameters represent the true values. We reject models at the 90% confidence level if $Q_{val} < 0.1$. Most sources have spectra that can be adequately described by an NEI model, a DBB model, or a combination of the two. In no case can a DBB contribution (i.e., both the DBB and DBB+NEI models) be ruled out at the 90% level. Thus, while a disk component is not strictly required, the spectra are consistent with the presence of a DBB component, which—given the observed variability—can be interpreted as evidence for an accretion disk.

6. Identifying Flux Components Associated with Variability

We now examine which spectral components are responsible for the observed variability in the high-probability variable sample. For sources with sufficient counts in more than one flux block, we compare spectra directly by fitting a DBB model to the lower-flux block (or blocks) and subtracting this model from the spectra of higher-flux block(s), thereby isolating the variable component. For all high-probability variable sources—including those with insufficient counts for reliable spectral fitting in individual blocks—we additionally examine their tracks in the flux-block diagrams (Section 4.1) to assess spectral behavior as a function of flux.

6.1. Fits to High- and Low-flux Blocks

We first focus on the subset of high-probability variable sources with adequate counts to perform spectral fitting in multiple flux blocks. For each source, we fit a DBB model to the lower-flux block(s) and subtract the resulting model from the higher-flux block(s) to reveal the residual emission. Individual flux blocks were included only if they contained $\gtrsim$30–40 counts; blocks with fewer counts do not provide enough dofs for reliable spectral fitting. When appropriate, adjacent blocks in the flux–color diagram—defined by overlapping flux and color uncertainties—were combined to improve the signal-to-noise ratio. The fitting approach parallels that described in Section 5, with two minor differences: (1) spectra were grouped to a minimum of seven

Table 4
Summary of Rejected Spectral Models

Source	Counts	Q_{val}(DBB)	Q_{val}(NEI)	Q_{val}(DBB+NEI)	Rejected Models
2CXOJ133648.3−295244	108.47	0.73	0.40	⋯	⋯
2CXOJ133649.7−295217	391.85	0.30	0.42	0.04	DBB+NEI
2CXOJ133650.8−295240	252.63	0.96	0.99	0.98	⋯
2CXOJ133650.9−295226	202.69	0.34	0.44	0.06	DBB+NEI
2CXOJ133652.8−295110	48.48	0.73	0.69	⋯	⋯
2CXOJ133652.8−295231	304.78	0.19	0.85	0.87	⋯
2CXOJ133653.2−295133	58.26	0.54	0.64	⋯	⋯
2CXOJ133653.8−294848	277.64	0.09	0.74	0.62	DBB
2CXOJ133654.1−295209	43.18	0.80	0.56	⋯	⋯
2CXOJ133654.8−295018	63.37	0.68	0.60	⋯	⋯
2CXOJ133655.0−295239	266.84	0.39	0.33	0.32	⋯
2CXOJ133655.1−295040	49.13	0.97	0.90	⋯	⋯
2CXOJ133655.5−295303	434.08	0.01	0.00	0.96	DBB, NEI
2CXOJ133656.2−295255	363.60	0.10	0.00	0.03	NEI, DBB+NEI
2CXOJ133657.8−295303	731.07	0.32	0.42	0.33	⋯
2CXOJ133658.5−294819	45.03	0.79	0.65	⋯	⋯
2CXOJ133658.7−295100	119.01	0.68	0.98	⋯	⋯
2CXOJ133659.3−294837	48.64	1.00	0.62	⋯	⋯
2CXOJ133659.3−295508	155.09	0.85	0.92	0.72	⋯
2CXOJ133659.5−295204	227.62	0.86	0.73	0.70	⋯
2CXOJ133659.8−295526	183.39	0.85	0.82	0.04	DBB+NEI
2CXOJ133700.1−294810	30.09	0.78	0.86	⋯	⋯
2CXOJ133700.4−295323	49.87	0.63	0.90	⋯	⋯
2CXOJ133701.0−295056	149.52	0.89	0.57	⋯	⋯
2CXOJ133701.6−295202	144.26	0.60	0.22	⋯	⋯
2CXOJ133701.7−295113	228.32	0.67	0.66	0.63	⋯
2CXOJ133702.2−294952	258.65	0.12	0.95	0.91	⋯
2CXOJ133702.4−295126	735.79	0.36	0.20	0.94	⋯
2CXOJ133703.0−294945	251.09	0.03	0.97	0.99	DBB
2CXOJ133703.4−295401	43.72	0.37	0.22	⋯	⋯
2CXOJ133703.5−294940	161.57	0.15	0.00	0.00	NEI, DBB+NEI
2CXOJ133706.1−295444	256.19	0.95	0.96	0.97	⋯
2CXOJ133706.4−295025	36.60	0.69	0.43	⋯	⋯
2CXOJ133706.6−295332	300.79	0.00	0.07	0.60	DBB, NEI
2CXOJ133707.0−295321	27.97	0.78	0.59	⋯	⋯
2CXOJ133708.3−295056	47.82	0.52	0.19	⋯	⋯
2CXOJ133708.5−295135	102.24	0.58	0.91	⋯	⋯
2CXOJ133708.7−295137	64.78	0.72	0.75	⋯	⋯
2CXOJ133710.0−295128	60.97	0.38	0.09	⋯	NEI
2CXOJ133710.9−295046	39.01	0.79	0.29	⋯	⋯
2CXOJ133711.8−295215	359.85	0.32	0.44	0.01	DBB+NEI
2CXOJ133712.0−295056	153.52	0.13	0.89	0.76	⋯
2CXOJ133712.4−295140	339.18	0.43	0.33	0.91	⋯

Note. The table lists the source identifier, the number of background-subtracted counts, and the goodness-of-fit statistic (Q_{val}) for the NEI, DBB, and combined DBB +NEI models. Models with $Q_{val} < 0.1$ are considered rejected and are listed in the final column.

counts per bin, and (2) the line-of-sight absorption was not allowed to vary in the fit and was fixed at $N_H = 3.7 \times 10^{20}$ cm^{-3}. The following residuals were generated:

1. *2CXOJ133702.4–295126*. Fit to Block 1 subtracted from Block 2.
2. *2CXOJ133655.5–295303*. Fit to Block 2 subtracted from Blocks 3+4 and fit to Block 1 subtracted from Block 5.
3. *2CXOJ133655.0*–295239. Fit to Block 1 subtracted from Block 2.
4. *2CXOJ133657.8*–295303. Fit to Block 1 subtracted from Block 2.
5. *2CXOJ133701.7*–295113. Fit to Block 1 subtracted from Block 3.
6. *2CXOJ133706.1*–295444. Fit to Blocks 1+2 subtracted from Blocks 4+5.

Table 5 summarizes the spectral fits to the individual blocks, with 1σ (68.27%) confidence intervals on T_{in} derived from the covariance method in `sherpa` (Section 5) and dof defined as the number of spectral bins minus the number of free parameters. The corresponding flux-block tracks and residual spectra are shown in Figures 7–12.

6.2. Tracks in the Flux-block Diagram

Not all sources in the high-probability variable sample have sufficient counts in individual flux blocks to permit reliable spectral fitting. For these sources, we instead use the flux-block diagrams to provide a qualitative indication of how the X-ray color—and thus the inferred spectral temperature—varies with flux. Figure 13 shows the flux-block diagrams for all high-probability variable sources. Several objects

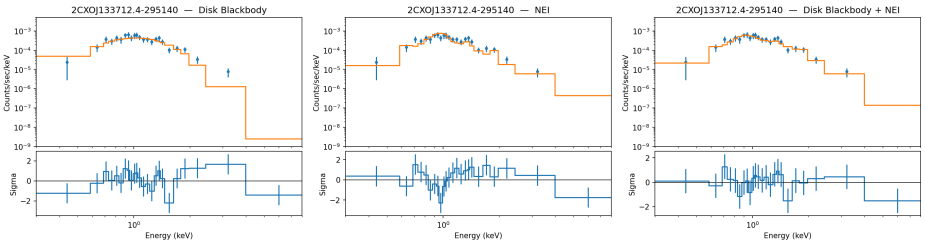

Figure 6. Fitted spectra for 2CXOJ133712.4−295140. From left to right: (1) the DBB model, (2) the NEI model, and (3) the combined DBB+NEI. The complete figure set (43 images) is available in the online journal.
(The complete figure set (43 images) is available in the online article.)

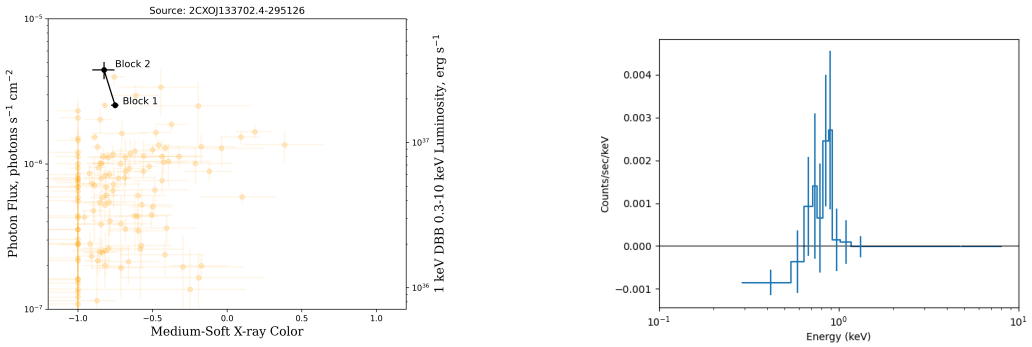

Figure 7. Flux-block diagram and spectral residuals for 2CXOJ133702.4–295126. Left: flux-block diagram for SNRs in the Q. Hunt et al. (2021) sample, with 2CXOJ133702.4–295126 highlighted. Right: residual spectrum obtained by subtracting the best-fit model for Block 1 from that of Block 2.

Table 5
Spectral Fits to Individual Flux Blocks for High-probability Variable Sources in Cases Where Individual Blocks Contain Sufficient Counts to Permit Spectral Fitting

Source	Counts	$T_{\rm in}$ (keV)	$T_{\rm in,min}$ (keV)	$T_{\rm in,max}$ (keV)	χ^2	dof	χ^2/dof
2CXOJ133702.4−295126							
Blk 1	658.90	0.27	0.26	0.28	69.77	59	1.18
2CXOJ133655.5−295303							
Blk 1	49.80	1.6	0.7	2.6	3.98	9	0.44
Blk 2	32.10	1.80	0.6	3.0	0.85	5	0.17
2CXOJ133655.0−295239							
Blk 1	73.40	0.19	0.17	0.22	6.35	11	0.58
2CXOJ133657.8−295303							
Blk 1	640.10	0.23	0.22	0.24	57.50	58	0.99
2CXOJ133701.7−295113							
Blk 1	146.90	0.23	0.21	0.26	12.71	20	0.64
2CXOJ133706.1−295444							
Blk 1+2	33.70	0.2	0.1	0.3	2.07	8	0.26

Note. The counts are background subtracted.

(2CXOJ133653.8−294848, 2CXOJ133655.0−295239, 2CXOJ133657.8−295303, 2CXOJ133648.3−295244, and 2CXOJ133653.2−295133) show hints of color evolution consistent with spectral hardening at higher fluxes. In some cases—notably 2CXOJ133653.8–294848—the track suggests an initial hardening followed by softening, tracing a backward "C" shape in the flux-block diagram.

In most sources, however, the change in color is modest: The hardness ratio typically varies by less than a factor of 2 across the observed flux range. The uncertainties are large and prevent firm conclusions about spectral evolution. Overall, the data are consistent with approximately constant X-ray color as the flux increases. Determining whether significant color changes occur in any subset of the population will require higher-quality data and a larger sample spanning multiple galaxies.

6.3. Components Driving Variability

Visual inspection of the high-flux residuals in Figures 7–12 shows that, in all cases, the excess emission is concentrated at energies around and below ∼1 keV, with no significant residuals above 2 keV. In the flux-block diagram, this behavior corresponds primarily to vertical motion—an increase in flux with little change in color. Similar trends are observed, albeit with large uncertainties, in the flux-block tracks of lower-count high-probability variable sources. As noted in Section 1, soft X-ray emission around ∼1 keV is characteristic of a cool accretion disk. While alternative interpretations cannot be ruled out, the ∼1 keV residuals are qualitatively consistent with variations in the accretion rate of a disk. Higher-quality data with greater photon statistics will be required to test this hypothesis quantitatively.

7. Origin of the Variability in SNRs

In this section, we explore the physical origin of the variability exhibited by X-ray sources associated with SNRs. As noted in Section 1, two scenarios are most plausible: (1) the remnants are intrinsically young and still evolving rapidly, or (2) the detected variability arises from an accreting compact object—for example fallback accretion or a HMXB in a star-

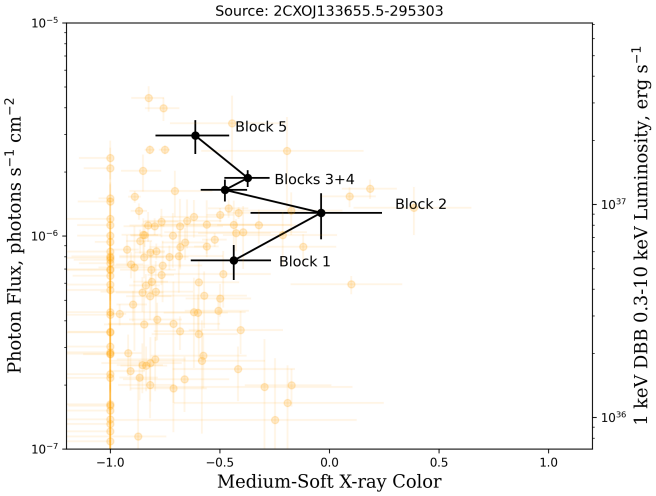

(a) Flux blocks

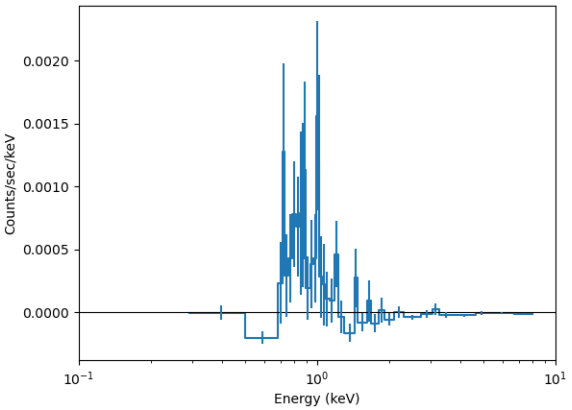

(b) Block-2 fit subtracted from Blocks 3+4

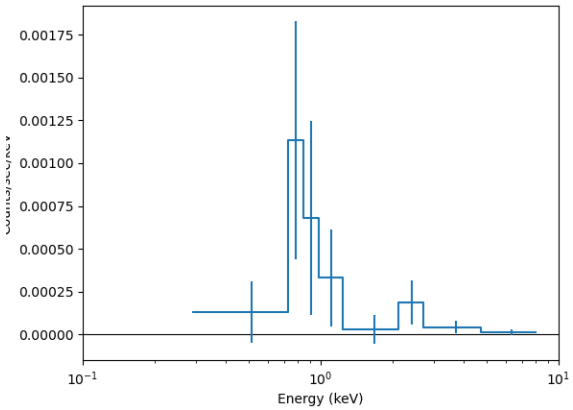

(c) Block 1 fit subtracted from Block 5

Figure 8. Flux-block diagram and spectral residuals for 2CXOJ133655.5–295303. Top: flux-block diagram. Bottom left: residual spectrum obtained by subtracting the best-fit model for Block 2 from that of Blocks 3+4. Bottom right: residual spectrum obtained by subtracting the best-fit model for Block 1 from that of Block 5.

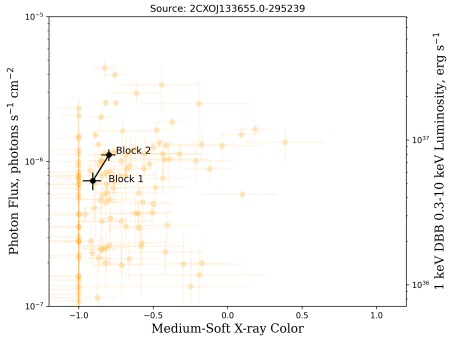

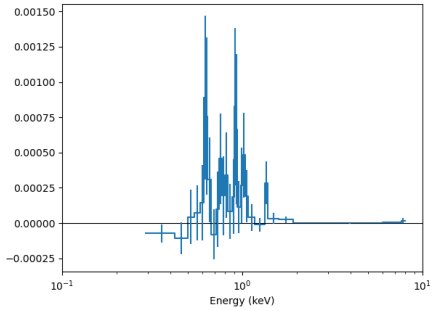

Figure 9. Flux-block diagram and spectral residuals for 2CXOJ133655.0–295239. Panels are as described in Figure 7.

forming environment—physically coincident with the remnant. We examine these possibilities below.

7.1. Variability Associated with Young SNe

Two of the SNRs—2CXOJ133703.5−294940 and 2CXOJ133706.6−295332 (B12-174a)—are identified as "young" (< 100 yr) by K. S. Long et al. (2022). Their flux-block tracks are shown in Figure 14.

Source 2CXOJ133703.5−294940 (associated with SN 1957D) does not fall into our high-probability variable sample but it is likely variable ($P_{\rm var}(b)$=0.67). Emission was detected in 2011 but fell below the detection threshold at other epochs. SN 1957D has been studied extensively by V. Ramakrishnan &

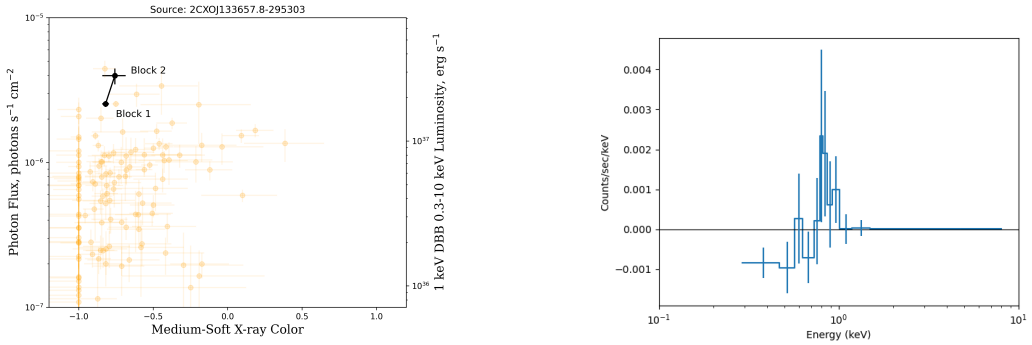

Figure 10. Flux-block diagram and spectral residuals for 2CXOJ133657.8–295303. Panels are as described in Figure 7.

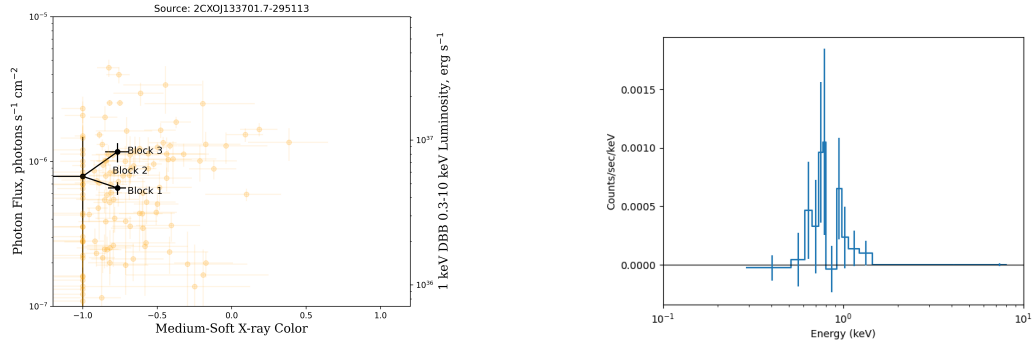

Figure 11. Flux-block diagram and spectral residuals for 2CXOJ133701.7–295113. Panels are as described in Figure 7.

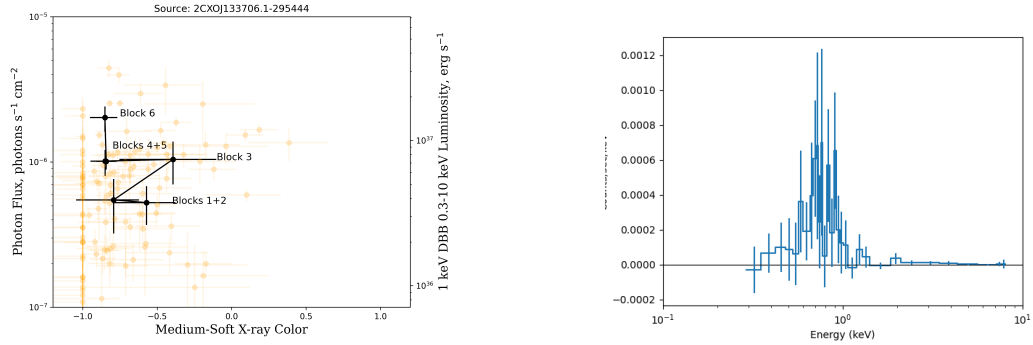

Figure 12. Flux-block diagram and spectral residuals for 2CXOJ133706.1–295444. Residual spectrum obtained by subtracting the best-fit model for Blocks 1+2 from those of Blocks 4+5.

V. V. Dwarkadas (2021), who attribute its spectral and temporal evolution to shock-heated ejecta, with the X-ray flux declining slowly as the SNe expands and cools. We agree that this is the most natural interpretation; however, we note that the spectrum is not well described by standard shock-heated thermal models (Table 3), a discrepancy also noted by V. Ramakrishnan & V. V. Dwarkadas (2021).

Source 2CXOJ133706.6−295332 also shows strong evidence for variability ($P_{\rm var}(b) = 0.94$). Its classification as "young" is based on the large widths of its optical emission lines (>1000 km s^{-1}; K. S. Long et al. 2022). Its X-ray light curve does not follow the smooth decline typically expected for young SNe. The flux appears to rise between 2000 and 2001 (albeit with large uncertainties) before declining, and may exhibit substantial fluctuations in 2011. Notably, the X-ray spectrum becomes softer as the source brightens, consistent with variability driven by an accretion disk rather than shock evolution. We therefore consider accretion a more plausible origin for the observed variability.

As discussed in Section 3, several additional sources display light curves that could be consistent with the slow, monotonic decline expected for young SNe, making it tempting to interpret the SD sources as young (<100 yr) SNe. However, an apparently smooth decline could instead arise from sparse temporal sampling of the Chandra observations, which may fail to capture episodes of flaring, and there is no independent evidence supporting a young SN origin for these sources. While we cannot rule out the possibility that some SD sources are young SNe, it is unlikely that evolution of the hot gas dominate this class.

7.2. Variability Due to Fallback Accretion

An alternative explanation for the observed variability is fallback accretion. As discussed in Section 1, fallback

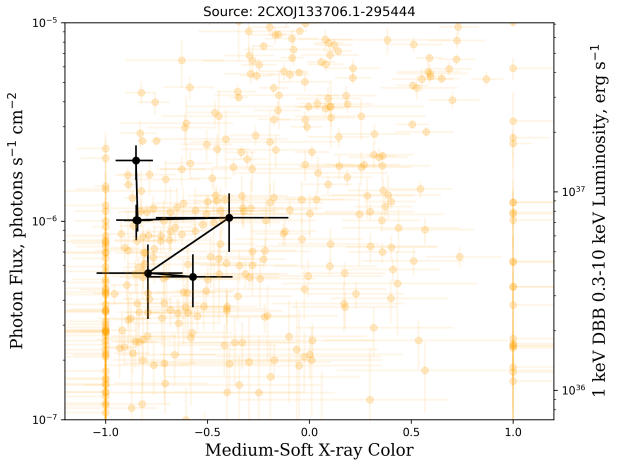

Figure 13. Flux-block plot for 2CXOJ133706.1−295444. The complete figure set for all high-probability variable sources (22 images) is available in the online journal.

(The complete figure set (22 images) is available in the online article.)

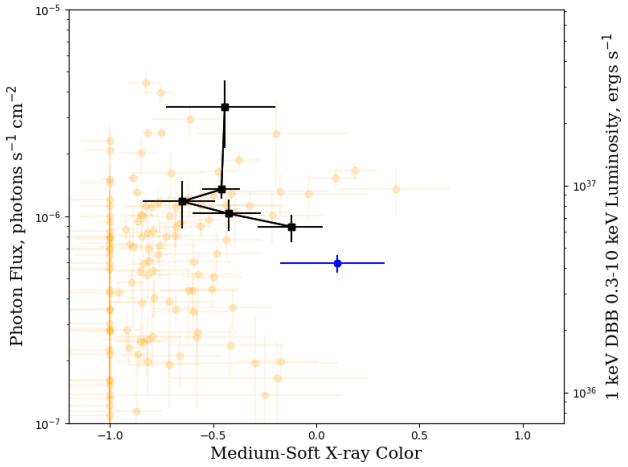

Figure 14. Supernova remnant flux-block diagram highlighting the tracks of two young SNe. The tracks of 2CXOJ133703.5−294940 (blue) and 2CXOJ133706.6−295332 (black) are emphasized. Source 2CXOJ133703.5−294940 is associated with the historical supernova SN 1957D.

accretion in the immediate aftermath of a SN explosion is expected to influence the early evolution of the newly formed neutron star or black hole. In this scenario, the X-ray emission originates from an accretion disk formed by SN ejecta that fails to escape and subsequently falls back onto the compact remnant. In contrast to the young systems for which fallback accretion models have been developed, the sources in our sample would require a residual accretion disk that remains active for hundreds to thousands of years after the explosion. Extending fallback accretion models from the days-to-weeks timescales following core collapse to such late epochs is highly speculative. Significant theoretical work is therefore needed to determine whether long-lived fallback accretion can be sustained at the inferred luminosities and reproduce the observed X-ray spectral properties over these timescales.

Despite these uncertainties, fallback accretion remains a plausible explanation for the unexpected variability observed in a subset of our sources. A potential example of a fallback accretion disk is the luminous X-ray source associated with SN 1979C ($L_X \approx 6.5 \times 10^{38}$ erg s^{-1}) in the nearby galaxy M100 (D. J. Patnaude et al. 2011). Although the central source in SN 1979C is significantly more luminous than those in our sample, it is also much younger, and its X-ray spectrum is qualitatively similar, consisting of two thermal components with temperatures of $kT \approx 0.75$ and 1.86 keV. We therefore speculate that SN 1979C could evolve into an object resembling those in our sample at later times. Within our sample, the most promising fallback accretion candidates are sources that are both relatively young and variable, and whose X-ray spectra are well described by a DBB component (e.g., 2CXOJ133706.6−295332).

7.3. Variability Due to HMXBs Associated with the SNRs

Another plausible explanation for the observed variability is the presence of an XRB associated with the remnant. If a significant fraction of the variable SNR population in M83 hosts HMXBs, one would expect massive stars—potential donor stars—to lie within the X-ray positional error circles. M83 is currently undergoing a starburst, and SNRs are preferentially located in regions of active star formation; consequently, massive stars are common in the vicinity of many X-ray sources. It is therefore impossible to unambiguously identify potential donor stars.

Nevertheless, it is possible to demonstrate statistically that SNR X-ray sources are associated with a stellar population that differs from that of nearby comparison regions, exhibiting a significantly higher fraction of high-mass stars and thus an enhanced likelihood of hosting potential donor stars. In this section, we (1) compare the density of stars near SNR X-ray sources with that in adjacent regions, and (2) use color–magnitude diagrams to obtain a qualitative picture of the masses and evolutionary states of the surrounding stellar population.

We queried Version 3 of the Hubble Source Catalog (HSC; STScI 2016; B. C. Whitmore et al. 2016) to identify stars in the vicinity of the X-ray sources and to measure the stellar surface density as a function of projected distance. Cone searches with a radius of 0.″7 were performed using "Catalogs.query_region" in the ASTROQUERY.MAST module of the Python `astroquery` package. To ensure data quality, we restricted the sample to HSC sources detected in at least two filters and observed in four or more separate exposures.

As a control, we generated a comparison sample by offsetting each X-ray source position by 10″ in a randomly chosen direction and repeating the cone search with the HSC. We then applied a two-sided Kolmogorov–Smirnov (KS) test to compare the radial distribution of stars around the true X-ray positions with that around these shuffled positions. This procedure was repeated 100 times, with independent random offsets in each realization, to obtain a representative set of trials.

Figure 15 shows the cumulative radial distributions for one representative realization, comparing stars near the real X-ray sources (blue) with those near the shuffled positions (orange). In this example, the null hypothesis that the two samples are drawn from the same parent distribution is rejected at high significance ($p = 0.02$), with a higher stellar density near the true X-ray positions. The distribution of p-values from all 100 realizations is shown in Figure 16. The predominance of low p-values suggests that the stellar density around the X-ray sources differs from that of the shuffled positions.

To further investigate the stellar populations surrounding the SNR X-ray sources, we follow the approach of Q. Hunt et al. (2021) and compare the observed stars with theoretical

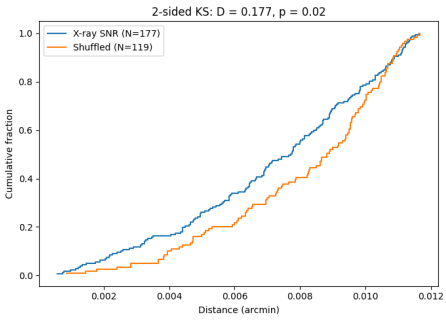

Figure 15. Fractional cumulative distribution functions for stars around real X-ray sources (blue) and shuffled sources (orange) obtained in a Kolmogorov–Smirnov (KS) test.

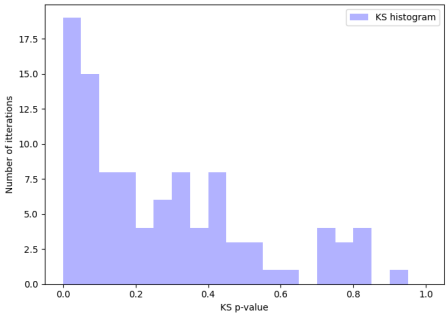

Figure 16. Histogram of p-values from 100 realizations of the Kolmogorov–Smirnov (KS) test comparing the distribution of stars around the real X-ray sources with that around shuffled positions. The distribution is skewed toward low p-values, indicating that in most realizations the stellar density near the real X-ray sources differs from that of the shuffled sample.

evolutionary mass tracks for solar-metallicity stars from the Padova PARSEC models (version 1.28; A. Bressan et al. 2012). Figure 17 presents the F814W–F438W color–magnitude diagram for HSCv3 sources, with evolutionary tracks for 5, 8, 20, and 40 $M_{\odot}$ stars overlaid. Stars associated with shuffled X-ray positions are shown in orange and provide a reference sample representative of the local stellar population, while stars located near the actual SNR X-ray sources are shown in blue.

Visual inspection suggests that the stellar population associated with the SNR X-ray sources contains a higher fraction of evolved stars with characteristic masses of ∼8–20 $M_{\odot}$ than is seen in the random comparison sample. Although there is overlap between the two populations, the distribution of stars near the SNR X-ray sources appears shifted toward higher masses and more evolved evolutionary stages. It is therefore important to consider whether systematic effects could produce an apparent difference between the stellar populations associated with the SNR X-ray sources and those around the shuffled comparison positions.

The plotted F814W–F438W colors and F814W magnitudes have not been corrected for extinction. As discussed by Q. Hunt et al. (2021), extinction shifts sources toward redder colors and fainter magnitudes in the color–magnitude diagram —that is, toward lower inferred masses. Extinction therefore cannot explain the apparent excess of massive, evolved stars near the SNR X-ray sources.

Differential extinction across M83 is also unlikely to be responsible. The galaxy exhibits a radial extinction gradient in which extinction is relatively low in the center, increases in the circumnuclear region, and then decreases in the disk (see Figure 2

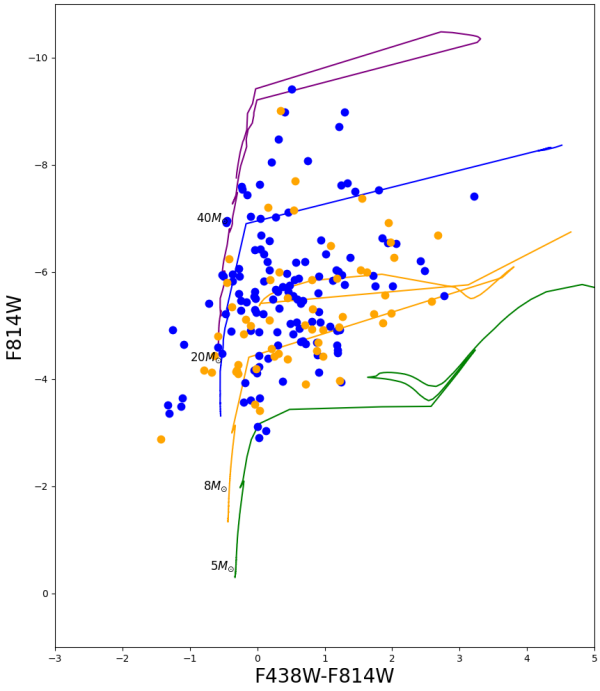

Figure 17. F814W/F438W color–magnitude diagram for HSCv3 sources. The evolutionary tracks for 5, 8, 20 and 40 $M_{\odot}$ stars are plotted. The orange points show the stars around the shuffled X-ray positions and the blue points show the stars around the actual X-ray sources

of S. Boissier et al. 2005). However, the 10″ positional offsets used to generate the shuffled sample are small compared to the spatial scale of this gradient, and the random directions of the offsets further reduce the likelihood of introducing a systematic extinction difference between the two samples.

Crowding may affect the detected stellar population if unresolved blends of faint stars appear as a single brighter source. If the SNR X-ray sources lie preferentially in dense stellar environments, such blending could bias detections toward brighter objects. However, an enhanced stellar density is expected if these sources are associated with star clusters or stellar associations, so this effect would reflect a genuine environmental difference rather than a spurious observational bias. That said, unresolved blends could in some cases alter the inferred photometric properties of individual objects—potentially shifting their apparent luminosities and colors and thus affecting the estimated stellar masses or evolutionary classifications.

Finally, differences in photometric completeness could in principle alter the inferred population if faint stars were systematically missed near the SNR positions but not at the shuffled locations. This appears unlikely because the offsets used to generate the comparison sample are small and randomly oriented, so the observational conditions affecting completeness should be similar for both samples.

From our investigation of the stellar populations surrounding SNR X-ray sources, we find that the stellar density in the immediate vicinity of the X-ray positions is higher than in nearby comparison regions, and that these populations include a relatively larger fraction of evolved, massive stars. We note that a similar association between HMXBs and evolved, massive stars was also reported by Q. Hunt et al. (2021). This indicates that the SNR X-ray sources are preferentially located in or near clusters containing massive stars. Given that core-collapse SNe arise from

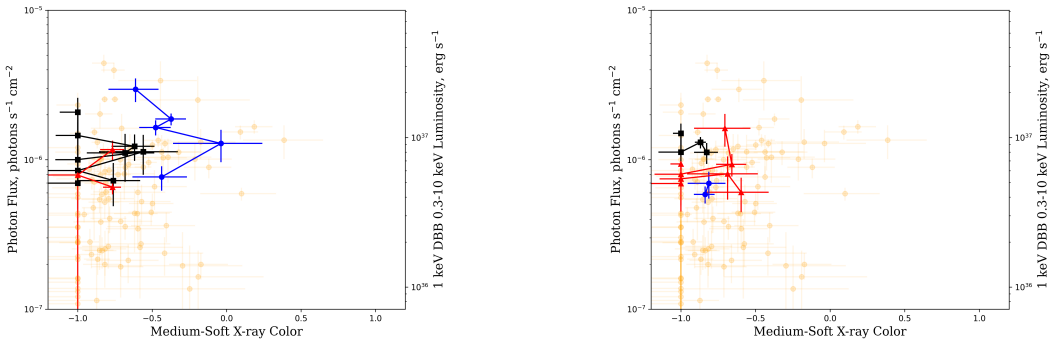
Photon Flux, photons s^{-1} cm^{-2}
1 keV DBB 0.3-10 keV Luminosity, erg s^{-1}
Medium-Soft X-ray Color
Photon Flux, photons s^{-1} cm^{-2}
1 keV DBB 0.3-10 keV Luminosity, erg s^{-1}
Medium-Soft X-ray Color

Figure 18. Location of microquasar candidates in the flux-block diagram. The left panel shows candidates that are likely variable: 2CXOJ133655.5−295303 (blue), 2CXOJ133659.5−295204 (black), and 2CXOJ133701.7−295113 (red). The source 2CXOJ133655.5−295303 was identified by R. Soria et al. (2020) as a microquasar candidate. The right panel shows candidates that have a lower probability of being variable: 2CXOJ133650.8−295240 (red), 2CXOJ133659.3−295508 (blue), 2CXOJ133711.8−295215 (black).

Table 6
Microquasar Candidates from R. Soria et al. (2020)

CSC ID	$P_{\rm var}(b)$	ID (W. P. Blair et al. 2015)	ID (R. Soria et al. 2020)
2CXOJ133650.8−295240	0.42	B12-045	S1
2CXOJ133655.5−295303	1.00	B12-098	S2
2CXOJ133659.3−295508	0.40	B12-122	S3
2CXOJ133659.5−295204	0.79	B12-124	S4
2CXOJ133701.7−295113	0.98	B12-143	S5
2CXOJ133711.8−295215	0.65	B12-209	S9

massive, evolved progenitors, this result is not unexpected. However, it also lends support to the HMXB interpretation by demonstrating that plausible high-mass donor stars are present close to the X-ray sources.

We conclude that the spatial distribution of stellar sources around SNR X-ray positions is inconsistent with that expected from randomly generated adjacent locations. In particular, there is an excess of stellar sources at small separations from the X-ray positions compared to the shuffled sample. In addition, the associated stellar population is dominated by evolved, massive stars, which are plausible donor-star candidates. Taken together, these results suggest that SNR X-ray sources are preferentially located in or near star clusters containing massive stars capable of serving as donors.

7.4. Association with Microquasar Candidates

A distinct subclass of HMXBs are microquasars, in which the compact object—most commonly a stellar-mass black hole—launches relativistic jets that interact with the surrounding ISM. Shocks driven by these jets can produce optical emission-line ratios that closely resemble those of SNRs. Motivated by this possibility, R. Soria et al. (2020) searched for elongated SNRs in M83 that might trace jet–ISM interactions and identified several candidates. They concluded that six of the microquasar candidates (S1, S3, S4, S5, S8, S9) are best interpreted as SNRs, based on their optical and infrared line ratios and the fact that the X-ray spectra are consistent with a thermal plasma with a temperature of $\sim$1 keV. They do not have enough data to explain the elongation of source S6, and S7 appears to be dominated by photoionization. They concluded that only one source, S2, shows strong evidence for a microquasar interpretation.

Several of the microquasar candidates identified by R. Soria et al. (2020) are included in our sample. These sources are listed in Table 6 and shown in the flux-block color diagram in Figure 18. To reduce visual confusion from overlapping tracks, we separate the candidates into two panels, distinguishing sources that are likely variable from those with lower variability probabilities.

The flux-block track and high-flux spectral residuals for 2CXOJ133655.5−295303 (S2) are shown in Figure 8. This source is strongly variable ($P_{\rm var}(b)$,=1.0), and its increasing flux is accompanied by excess emission at low energies. R. Soria et al. (2020) noted that its X-ray spectrum is harder than those of the other candidates, which are characterized by very soft, SNR-like spectra. This is confirmed by Figure 18, which clearly shows that 2CXOJ133655.5−295303 has a significantly harder spectrum than the other microquasar candidates. R. Soria et al. (2020) also noted that 2CXOJ133655.5−295303 exhibits significant variability. These properties formed the basis for their identification of 2CXOJ133655.5−295303 as a likely microquasar.

We note that 2CXOJ133701.7−295113 (S5) is included in our high-probability variable sample, while 2CXOJ133659.5−295204 (S4) has $P_{\rm var}(b) = 0.79$, just below our adopted high-probability variable threshold ($\geqslant$0.8). R. Soria et al. (2020) did not comment on variability in these sources. Because strong X-ray variability is a defining characteristic of microquasars, this motivates a reexamination of whether 2CXOJ133701.7−295113 and 2CXOJ133659.5−295204 are viable microquasar candidates.

We find that both a DBB model and a combined DBB+NEI model provide acceptable fits to the X-ray spectra of these sources. The presence of an accretion disk is therefore consistent with the X-ray data, although a purely thermal NEI interpretation cannot be excluded. R. Soria et al. (2020) also report that both objects exhibit elongated bipolar radio emission, which they interpret as a SN shock expanding into an asymmetric circumstellar medium. However, bipolar radio morphology is also qualitatively consistent with jet–ISM interactions expected in microquasar systems. Taken together—the observed variability and the bipolar radio structure

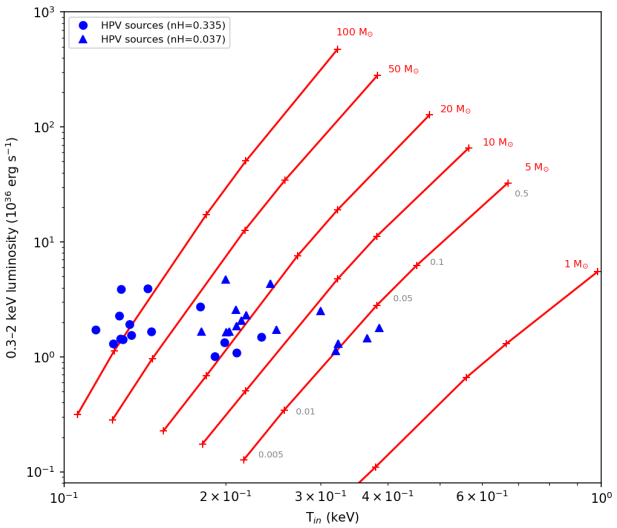

Figure 19. Absorbed luminosity vs. inner disk temperature for the sources most likely to be accretion powered. Circles show values derived using the adopted $N_{\rm H}$, while triangles correspond to fits assuming Galactic $N_{\rm H}$. Theoretical tracks for accreting black holes of different masses and accretion rates are overlaid.

—these properties suggest that 2CXOJ133701.7−295113 and 2CXOJ133659.5−295204 are plausible microquasar candidates, in addition to 2CXOJ133655.5−295303. Additional microquasars may also be present in the sample but remain unrecognized if the jet orientation does not produce clearly elongated, shock-excited nebulae. Confirming a microquasar identification at the distance of M83 is extremely challenging. One possible approach would be deep radio observations to search for jet structures and to monitor the sources for variability.

7.4.1. A Population of High-mass Black Hole X-Ray Binaries?

As discussed in Section 1, X-ray emission in black hole binaries typically originates from a relatively cool (10^6–10^7 K) accretion disk (N. I. Shakura & R. A. Sunyaev 1973; R. A. Remillard & J. E. McClintock 2006). The presence of soft residuals correlated with increased flux in the variable sources is similar to emission from such a disk. Motivated by this similarity, we explore the possibility that the SNR accretion sources are powered by black hole X-ray binaries.

Simple models of accretion disks predict that the temperature of the DBB emission scales as $M_{\rm BH}^{-1/2}$, where $M_{\rm BH}$ is the black hole mass (K. Ebisawa et al. 1991). This scaling holds if the inner edge of the disk lies near the innermost stable circular orbit (ISCO). If the X-ray emission originates from accretion onto black holes, we would expect the measured disk temperatures to be consistent with those of stellar-mass black holes.

The most plausible accretion-powered systems in our SNR sample are those in the high-probability variable subset. To minimize contamination from young SNe, we restrict the sample to sources that do not exhibit SD-type light curves. Figure 19 shows the absorbed 0.3–2 keV luminosity of the DBB component for these candidate accretion sources plotted as a function of the fitted inner disk temperature. Overlaid are theoretical tracks for black holes of different masses and Eddington-scaled accretion rates, following I. Galiullin & M. Gilfanov (2021). These tracks are computed using the general relativistic accretion disk (or GRAD) model for a nonrotating (Schwarzschild) black hole (K. Ebisawa et al. 1991), as implemented in XSPEC. All tracks show absorbed luminosities.

To illustrate the effect of the assumed $N_{\rm H}$, Figure 19 shows results derived using our adopted value (circles) and the Galactic value (triangles). The effect of increasing $N_{\rm H}$ is to shift the inferred parameters toward lower $T_{\rm in}$, and hence toward higher black hole mass tracks. If the adopted $N_{\rm H}$ is appropriate, several sources have $T_{\rm in}$ values that imply black hole masses in the range ∼50–100 $M_{\odot}$, at the upper end of what is typically expected from single core-collapse events. We also note that if the accretion disks are truncated and do not extend to the ISCO, the inferred $T_{\rm in}$ will be underestimated. Taking these uncertainties into account, the observed $T_{\rm in}$ values are broadly consistent with emission from a cool accretion disk around a stellar-mass black hole.

8. Summary and Conclusions

We find that a significant fraction of the soft X-ray sources associated with SNRs in M83 exhibit significant variability. This behavior is unexpected, as the soft X-ray emission from SNRs older than ∼100 yr is generally assumed to evolve smoothly, with little variation on decade-long timescales. The variable X-ray emission associated with SNRs in M83 likely arises from multiple physical mechanisms. At least one source in our sample, 2CXOJ133703.5−294940, is associated with the historical supernova SN 1957D. In this case, both the X-ray emission and its variability are well explained by shock interaction between the expanding ejecta and the surrounding circumstellar medium. For the majority of the variable sources, however, the observed behavior is more naturally interpreted as arising from a coincident accretion-powered source rather than from the intrinsic evolution of the SNR itself.

The nature of these accretion sources cannot be uniquely constrained with the current data. Plausible explanations include fallback accretion onto a compact object formed in the SN explosion, as well as X-ray binaries physically associated with the remnants. We explore the latter possibility in detail. The X-ray sources associated with SNRs are statistically correlated with high-mass stars, indicating the presence of potential donor stars and lending support to an HMXB interpretation. Moreover, the X-ray luminosities and spectral properties of these sources are broadly consistent with emission from cool accretion disks around stellar-mass black holes. At least one source in our sample, 2CXOJ133655.5−295303, has previously been identified as a microquasar, and additional systems of this type may be present but remain unrecognized if their jet geometry does not produce a clearly elongated or extended nebula.

8.1. Implications and Suggestions for Further Work

The principal observational result of this study is the detection of significant X-ray variability in a substantial fraction of the SNR population in M83. In most cases, the variability is more plausibly attributed to a coincident accretion-powered source than to intrinsic evolution of the remnant. This has important implications for interpreting X-ray emission from SNRs: The observed flux may represent only an upper limit on thermal emission from shock-heated gas and, in some cases, may be dominated by an accretion component. Consequently, existing luminosity functions for extragalactic SNRs may require revision to account for contamination by variable accreting sources.

If the variable SNR population in M83 is dominated by HMXBs, this would imply an unusually large number of such systems in this galaxy. While HMXBs associated with SNRs are known in the Milky Way and the Magellanic Clouds (F. D. Seward et al. 2012; R. H. D. Corbet et al. 2016), they are relatively rare and their formation pathways remain uncertain (Z.-P. Xing & X.-D. Li 2021; A. D. Khokhriakova & S. B. Popov 2022). Given the youth of the remnants, such a population would suggest a substantial number of young, nearly coeval X-ray binaries—possibly hosting black holes. An apparent excess of these systems may be related to the recent starburst history of M83, which could favor the formation of otherwise uncommon accreting binaries.

Clarifying the nature of these sources will require systematic searches for variable, accretion-powered X-ray sources located near SNRs in the Milky Way and Local Group galaxies. In M83, the remnants are not spatially resolved by Chandra. Identifying soft, variable X-ray sources in close proximity to SNRs in nearby galaxies would therefore provide a more direct test of whether the emission arises from an associated accretion source.

Further progress will also require detailed studies of the stellar environments surrounding these X-ray sources to identify potential donor stars. Such analyses should evaluate candidate counterparts on a source-by-source basis and place constraints on the masses of possible donors. In parallel, theoretical work is needed to assess whether fallback accretion can plausibly account for the observed variability and spectral properties on the relevant timescales.

Finally, improved constraints on long-term variability will require additional high-spatial-resolution soft X-ray observations. Future high-resolution X-ray observatories with improved sensitivity will allow more precise measurements of spectral variability and help distinguish accretion-powered emission from thermal emission associated with the remnants.

Acknowledgments

The authors thank the X-ray Galaxies Group at NASA Goddard Space Flight Center, in particular Ann Hornschemeier, Mihoko Yukita, and Antara R. Basu-Zych, for their encouragement and insightful discussions. We also acknowledge Qiana Hunt, Dan Castro, Brian Williams, Bret Lehmer, and Steven Saar for their valuable input and conversations. A.H.P. gratefully acknowledges the Chandra X-ray Center Helpdesk for their prompt and helpful assistance.

This work is supported by NASA under award No. 80GSFC24M0006.

This research has made use of data obtained from the Chandra Source Catalog, provided by the Chandra X-ray Center (CXC). This research employs a list of Chandra datasets, obtained by the Chandra X-ray Observatory, contained in doi:10.25574/cdc.572.

Based on observations made with the NASA/ESA Hubble Space Telescope and obtained from the Hubble Legacy Archive, which is a collaboration between the Space Telescope Science Institute (STScI/NASA), the Space Telescope European Coordinating Facility (ST-ECF/ESAC/ESA), and the Canadian Astronomy Data Centre (CADC/NRC/CSA).

This work has made use of the Padova Stellar Tracks and Isochrones database (http://stev.oapd.inaf.it).

This material is based upon work while AHP was serving at the National Science Foundation.

AHP acknowledges the use of ChatGPT to format tables and proofread the manuscript.

Facilities: CXO, HST.

Software: Astropy (Astropy Collaboration et al. 2013, 2018, 2022), CIAO (https://cxc.cfa.harvard.edu/ciao/; A. Fruscione et al. 2006), `Sherpa` (https://cxc.cfa.harvard.edu/sherpa/; A. Siemiginowska et al. 2024), TOPCAT (https://www.star.bristol.ac.uk/mbt/topcat/; M. B. Taylor 2020).

Appendix
Source List and Variability Indices

Table 7 in this Appendix contains the primary SNR sources used in this paper.

Table 7
Primary Sample of SNRs used in this Paper

HuntID	CSCID	R.A.	Decl.	$P_{var}(b)$	$P_{var}(s)$
L19X269	2CXOJ133702.2−294952	204.25921318648057	−29.831239628649115	0.16	0.17
L19X048	2CXOJ133648.3−295244	204.2012559202591	−29.879113803439996	0.75	0.81
L19X056	2CXOJ133649.7−295217	204.20748254542514	−29.871510407217603	0.45	0.21
L19X066	2CXOJ133650.8−295240	204.2119559909322	−29.877838705945276	0.42	0.53
L19X068	2CXOJ133650.9−295226	204.21237972208166	−29.87393588887466	0.75	0.65
L19X095	2CXOJ133652.8−295110	204.22009269445493	−29.853011174996432	0.94	0.6
L19X094	2CXOJ133652.8−295231	204.22010821888762	−29.875497885943055	0.54	0.37
L19X106	2CXOJ133653.2−295133	204.22170635446332	−29.859411788217642	1.0	1.0
L19X116	2CXOJ133653.8−294848	204.22452014131113	−29.813472490708257	0.88	0.49
L19X121	2CXOJ133654.1−295209	204.22560954897642	−29.869300524836547	0.75	0.68
L19X131	2CXOJ133654.8−295018	204.22860735271752	−29.83856171804904	0.76	0.77
L19X132	2CXOJ133655.0−295239	204.2292859721814	−29.87767688131925	0.87	0.41
L19X135	2CXOJ133655.1−295040	204.22979452375193	−29.8445260651327	0.8	0.8
L19X144	2CXOJ133655.5−295303	204.23153258987372	−29.884364504889053	1.0	0.87
L19X149	2CXOJ133656.2−295255	204.23427307072996	−29.88205056393748	0.5	0.02
L19X171	2CXOJ133657.8−295303	204.2411586786916	−29.884164195125308	0.81	0.13
L19X180	2CXOJ133658.5−294819	204.24397325084738	−29.80550323116009	0.25	0.24
L19X185	2CXOJ133658.7−295100	204.24459791938966	−29.850167250858675	0.84	0.42
L19X196	2CXOJ133659.3−294837	204.2472774302131	−29.810416855430226	0.42	0.29
L19X195	2CXOJ133659.3−295508	204.2472410393931	−29.919113213241626	0.4	0.48
L19X201	2CXOJ133659.5−295204	204.2479134801913	−29.867797505311696	0.79	0.73
L19X209	2CXOJ133659.8−295526	204.24936440670308	−29.92398914129477	0.82	0.58

Table 7
(Continued)

HuntID	CSCID	R.A.	Decl.	$P_{var}(b)$	$P_{var}(s)$
L19X219	2CXOJ133700.1−294810	204.2507800666399	−29.802765080306678	0.52	0.45
L19X225	2CXOJ133700.4−295323	204.25170650920666	−29.889804171043295	0.83	0.9
L19X245	2CXOJ133701.0−295056	204.254263385346	−29.849003315592512	0.78	0.67
L19X257	2CXOJ133701.6−295202	204.25672146268266	−29.867243898400762	0.65	0.74
L19X262	2CXOJ133701.7−295113	204.25724943626824	−29.853753872826147	0.98	0.84
L19X275	2CXOJ133702.4−295126	204.26010286365226	−29.857268682658805	0.88	0.25
L19X285	2CXOJ133703.0−294945	204.262567541625	−29.829324396582276	0.39	0.14
L19X289	2CXOJ133703.4−295401	204.26451865803097	−29.90044196941877	0.85	0.87
L19X292	2CXOJ133703.5−294940	204.2649045141942	−29.82803974989558	0.67	0.47
L19X327	2CXOJ133706.1−295444	204.27573648305656	−29.91229608020869	1.0	0.95
L19X328	2CXOJ133706.4−295025	204.27683686644787	−29.84038877129614	0.83	0.81
L19X330	2CXOJ133706.6−295332	204.27769940855876	−29.892458113359076	0.94	0.84
L19X335	2CXOJ133707.0−295321	204.2794637193981	−29.88921029798822	0.76	0.83
L19X354	2CXOJ133708.3−295056	204.28468363876857	−29.848998454015938	0.59	0.82
L19X358	2CXOJ133708.5−295135	204.285705525205	−29.859747923981494	0.84	0.74
L19X361	2CXOJ133708.7−295137	204.28655047589416	−29.86040471632987	0.93	0.94
L19X373	2CXOJ133710.0−295128	204.29202078979563	−29.857846666074753	0.56	0.19
L19X378	2CXOJ133710.9−295046	204.29572344430858	−29.8462232375939	0.8	0.64
L19X383	2CXOJ133711.8−295215	204.29952217840116	−29.870986316111434	0.65	0.42
L19X385	2CXOJ133712.0−295056	204.3001965980419	−29.84911788700348	0.68	0.67
L19X390	2CXOJ133712.4−295140	204.30185188242194	−29.861158138501366	0.59	0.48

ORCID iDs

Nanda Rea https://orcid.org/0000-0003-2177-6388

References

Adamo, A., Kruijssen, J. M. D., Bastian, N., Silva-Villa, E., & Ryon, J. 2015, MNRAS, 452, 246
Antoniou, V., Hatzidimitriou, D., Zezas, A., & Reig, P. 2009, ApJ, 707, 1080
Astropy Collaboration, Price-Whelan, A. M., Lim, P. L., et al. 2022, ApJ, 935, 167
Astropy Collaboration, Price-Whelan, A. M., Sipőcz, B. M., et al. 2018, AJ, 156, 123
Astropy Collaboration, Robitaille, T. P., Tollerud, E. J., et al. 2013, A&A, 558, A33
Blair, W. P., Winkler, P. F., Long, K. S., et al. 2015, ApJ, 800, 118
Boissier, S., Gil de Paz, A., Madore, B. F., et al. 2005, ApJL, 619, L83
Borkowski, K. J., Lyerly, W. J., & Reynolds, S. P. 2001, ApJ, 548, 820
Bressan, A., Marigo, P., Girardi, L., et al. 2012, MNRAS, 427, 127
Chakraborti, S., Ray, A., Smith, R., et al. 2016, ApJ, 817, 22
Chandar, R., Johns, P., Mok, A., et al. 2020, ApJ, 890, 150
Chevalier, R. A. 1989, ApJ, 346, 847
Corbet, R. H. D., Chomiuk, L., Coe, M. J., et al. 2016, ApJ, 829, 105
Dexter, J., & Kasen, D. 2013, ApJ, 772, 30
Di Stefano, R., Kong, A. K. H., Greiner, J., et al. 2004, ApJ, 610, 247
Done, C., & Kubota, A. 2006, MNRAS, 371, 1216
Ebisawa, K., Mitsuda, K., & Hanawa, T. 1991, ApJ, 367, 213
Evans, I. N., Evans, J. D., Martínez-Galarza, J. R., et al. 2024, ApJS, 274, 22
Fragos, T., Andrews, J. J., Bavera, S. S., et al. 2023, ApJS, 264, 45
Fragos, T., Lehmer, B., Tremmel, M., et al. 2013, ApJ, 764, 41
Fruscione, A., McDowell, J. C., Allen, G. E., et al. 2006, SPIE, 6270, 62701V
Fürst, F., Kretschmar, P., Grinberg, V., et al. 2019, AN, 340, 323
Galiullin, I., & Gilfanov, M. 2021, A&A, 646, A85
Gibson, S. L., Wynn, G. A., Gompertz, B. P., & O'Brien, P. T. 2018, MNRAS, 478, 4323
Gierliński, M., & Done, C. 2003, MNRAS, 342, 1083
Gierliński, M., & Done, C. 2004, MNRAS, 347, 885
Hunt, Q., Gallo, E., Chandar, R., et al. 2021, ApJ, 912, 31
Immler, S., Fesen, R. A., Van Dyk, S. D., et al. 2005, ApJ, 632, 283
Janka, H.-T. 2012, ARNPS, 62, 407
Khokhriakova, A. D., & Popov, S. B. 2022, MNRAS, 511, 4447
Kilgard, R. E., Kaaret, P. E., Krauss, M. I., et al. 2001, BAAS, 199, 1349
Kyer, R., Albrecht, S., Williams, B. F., et al. 2024, ApJ, 961, 168
Lazzarini, M., Hinton, K., Shariat, C., et al. 2023, ApJ, 952, 114
Lehmer, B. D., Monson, E. B., Eufrasio, R. T., et al. 2024, ApJ, 977, 189
Lehmer, B. D., Wik, D. R., Hornschemeier, A. E., et al. 2013, ApJ, 771, 134
Long, K. S. 2017, in Handbook of Supernovae, ed. A. W. Alsabti & P. Murdin (Springer), 2005
Long, K. S., Blair, W. P., Winkler, P. F., et al. 2010, ApJS, 187, 495
Long, K. S., Blair, W. P., Winkler, P. F., et al. 2022, ApJ, 929, 144
Long, K. S., Kuntz, K. D., Blair, W. P., et al. 2014, ApJS, 212, 21
Maccarone, T. J., Yukita, M., Hornschemeier, A., et al. 2016, MNRAS, 458, 3633
Maddox, L. A., Cowan, J. J., Kilgard, R. E., et al. 2006, ApJ, 132, 310
McClintock, J. E., & Remillard, R. A. 2006, in Compact Stellar X-Ray Sources, ed. W. H. G. Lewin & M. van der Klis, 39 (Cambridge Univ. Press), 157
Michel, F. C. 1988, Natur, 333, 644
Misra, D., Kovlakas, K., Fragos, T., et al. 2023, A&A, 672, A99
Mitsuda, K., Inoue, H., Koyama, K., et al. 1984, PASJ, 36, 741
Patnaude, D. J., Loeb, A., & Jones, C. 2011, NewA, 16, 187
Prestwich, A. H., Kilgard, R. E., Primini, F., McDowell, J. C., & Zezas, A. 2009, ApJ, 705, 1632
Ramakrishnan, V., & Dwarkadas, V. V. 2020, ApJ, 901, 119
Ramakrishnan, V., & Dwarkadas, V. V. 2021, RNAAS, 5, 191
Remillard, R. A., & McClintock, J. E. 2006, ARA&A, 44, 49
Ronchi, M., Rea, N., Graber, V., & Hurley-Walker, N. 2022, ApJ, 934, 184
Saha, A., Thim, F., Tammann, G. A., Reindl, B., & Sandage, A. 2006, ApJS, 165, 108
Sasaki, M., Pietsch, W., Haberl, F., et al. 2012, A&A, 544, A144
Seward, F. D., Charles, P. A., Foster, D. L., et al. 2012, ApJ, 759, 123
Shakura, N. I., & Sunyaev, R. A. 1973, A&A, 24, 337
Siemiginowska, A., Burke, D., Günther, H. M., et al. 2024, ApJS, 274, 43
Soria, R., Blair, W. P., Long, K. S., Russell, T. D., & Winkler, P. F. 2020, ApJ, 888, 103
Stockdale, C. J., Maddox, L. A., Cowan, J. J., et al. 2006, AJ, 131, 889
STScI 2016, Hubble Source Catalog, STScI/MAST, doi:10.17909/T97P46
Talbot, R. J., Jr., Jensen, E. B., & Dufour, R. J. 1979, ApJ, 229, 91
Taylor, M. B. 2020, ASPC, 522, 67
Wang, L. J., Wang, X. F., Wang, S. Q., et al. 2018, ApJ, 865, 95
Whitmore, B. C., Allam, S. S., Budavári, T., et al. 2016, AJ, 151, 134
Winkler, P. F., Blair, W. P., & Long, K. S. 2017, ApJ, 839, 83
Wofford, A., Leitherer, C., & Chandar, R. 2011, ApJ, 727, 100
Xing, Z.-P., & Li, X.-D. 2021, ApJ, 920, 67